A cascade-looped thermoacoustic driven cryocooler with different-diameter resonance tubes. Part II: Experimental study and comparison

Jingyuan Xu[a,b], Jianying Hu[a*], Yanlei Sun[a], Huizhi Wang[a], Zhanghua Wu[a], Jiangfeng Hu[a], Ercang Luo[a*], Simone Hochgreb[b],

a. CAS Key Laboratory of Cryogenics, Technical Institute of Physics and Chemistry, Chinese Academy of Sciences, Beijing 100190, China

b. Department of Engineering, University of Cambridge, Cambridge CB2 1PZ, United Kingdom

Abstract

A small-scale, heat-driven cooling system is required for on-site liquefaction of unconventional natural gas in a distributed station. To meet such demands, we propose a highly efficient heat-driven thermoacoustic cryocooler. This paper presents the experimental results of the proposed system, which is optimized based on previous theoretical analysis. Firstly, we compare two high-temperature heat exchangers with similar heat transfer effectiveness but different flow uniformity. The experimental results show that the heat exchanger with uniform flow can improve system efficiency by 28%. Experimental investigations are then carried out to understand the effect of operating temperatures on system performance. Later, the performance of the system operating at variable heating temperatures is studied. Finally, the reasons for the discrepancy between experiments and calculations are discussed. The experimental results show that the proposed thermoacoustically-driven cryocooler can achieve an exergy efficiency of 10 % and a cooling power of 378 W at a heating temperature of 730 K and a cooling temperature of 130 K. This represents a 25% improvement in efficiency compared to the previous record-holder thermoacoustic system.

* Corresponding author. Tel/Fax: +86 10 82543750 E-mail: ecluo@mail.ipc.ac.cn (E. Luo)
Tel/Fax: +86 10 82543733 E-mail: jyhu@ mail.ipc.ac.cn (J. Hu)

Keywords

Thermoacoustic engine; Thermoacoustic; Thermoacoustic cryocooler; Stirling

1 Introduction

Natural gas has been the fastest-growing energy resource in most regions of the world for over two decades, driven by low greenhouse gas emissions as well as high conversion efficiency in power generation [1]. For almost a century, natural gas has been reliably transported by pipelines from easily reachable locations. Recently, unconventional gas (principally shale gas, coal-bed methane, and tight gas) has gained much interest due to its potential contribution to gas production, as a result of developments in extraction technology. In the US, shale gas rose from only 2% of national production in 2000 to 20% in 2010 and is forecast to continue to rise to more than 46% by 2035 [2]. However, significant quantities of unconventional gas are inaccessibly located in isolated and remote areas, where current pipeline transport may be uneconomical. Under these conditions, it may be advantageous to liquefy the unconventional natural gas in producing regions and transport it via tanker truck or freight ship to consumption regions. However, conventional liquefaction processes based on mixed refrigerant, turbo-expander, and cascade cycles [3-6] are too large to be compatible with such small-scale, distributed applications. Furthermore, these liquefaction processes largely rely on electric power which is often not available in remote areas. Therefore, developing a small-scale heat-driven cryocooler can satisfy an important need for distributed natural gas stations.

Energy conversion based on thermoacoustic effects promises novel sustainable heat-driven technologies that can be applied to heating [7], cooling [8-10], and power generation [11-13]. A thermoacoustically-driven cooler (TADC) works by converting thermal energy into acoustic power necessary to pump heat from lower to higher temperatures, offering a promising solution to the above-mentioned problem. The ability to utilize the thermal energy that arises from burning a small amount of natural gas to liquefy a large amount of natural gas makes TADC very attractive for distributed applications. Furthermore, the TADC involves no harmful ozone-depleting gases and no mechanical moving components, providing an environmentally friendly and reliable cooling solution. A TADC consists of a thermoacoustic heat engine coupled to a thermoacoustic cooler. The development of TADC closely depends on the development of the thermoacoustic engine. According to the phase relationship between the pressure wave and volume flow rate in regenerator and resonance tube, the thermoacoustic engines have been developed into three generations: (1) The first generation thermoacoustic engine is a double standing-wave type where the regenerator and the resonance tube are both dominated by standing-wave fields [14-17]. Its thermal efficiency is limited to about 20% [18] because it works on an intrinsically irreversible

thermodynamic cycle; (2) The second generation thermoacoustic engine is a standing-traveling-wave hybrid type where the regenerator and the resonance tube are dominated by traveling-wave and standing-wave fields, respectively [19]. Although the thermal efficiency of this engine is increased to more than 30% [19,20], the non-compact size and low power density resulting from large-volume resonance tubes still limit its further applications; (3) The third generation thermoacoustic engine is a looped traveling-wave type [21-23], where the regenerator and the resonance tube are both dominated by traveling-wave fields. This novel thermoacoustic engine is characterized by compact size, large power density, and high potential efficiency and has become the focus of intensive research.

Based on the above three generations of thermoacoustic engines, some efforts have been made to develop TADCs for natural gas liquefaction. In 1998, a double standing-wave type TADC (first generation) was developed, which achieved a cooling power of 2.1 kW and an overall exergy efficiency of 5.8 % at a cooling temperature of 125 K [24]. Later, Praxair Inc. and Los Alamos National Laboratory jointly developed a standing-traveling-wave hybrid type TADC (second generation) which reached 3.8 kW of cooling power at a cooling temperature of 150 K [25]. Developments in high-efficient TADC natural gas liquefiers were accelerated by the development of the looped traveling-wave thermoacoustic engine (third generation). In 2015, a looped traveling-wave TADC operating at natural gas liquefaction temperatures was developed [26,27]. Experimental results showed that this system achieved a record exergy efficiency of 8 % and an overall cooling power of 1.2 kW at 130 K, which was capable of liquefying 65% of the natural gas while burning 35% natural gas.

While several major breakthroughs have been reported in the TADCs for natural gas liquefaction, their commercial application still seems far from being accomplished due to the relatively low efficiencies. To overcome this limitation, we propose a highly-efficient TADC via the introduction of the following concepts: (i) use resonance tubes with different diameters in order to match the acoustic impedance; (ii) incorporate thermoacoustic engines and coolers in a loop to recover acoustic power; (iii) employ a heat exchanger with uniform flow to reduce exergy loss caused by jet-driven streaming. A detailed theoretical analysis of the proposed system can be found in Ref. 28. The present paper provides a detailed experimental study as well as comparisons with the calculation results.

2 Experimental Setup and Measurements

2.1 Experimental setup

Figure 1 shows the schematic and experimental setup of the system. In this configuration, three thermoacoustic engine units and two parallel thermoacoustic cooler units are connected in a loop by different-diameter resonance tubes. The thermoacoustic engine unit, shown schematically in Figure 1c, consists of a main ambient heat exchanger (MAHX), a regenerator (REG), a high-temperature heat exchanger (HHX), a thermal buffer tube (TBT), and a secondary ambient heat exchanger (SAHX). The thermoacoustic cooler unit, shown schematically in Figure 1d, consists of a MAHX, a REG, a cold-temperature heat exchanger (CHX), a pulse tube (PT), and a flow straightener (FS). Based on the optimization design in Ref. 28, the dimensions of the main components of the system are listed in Table 1. It is noted that the total flow area of the two cooler units is close to the optimal designed area, and the area ratio of the adjacent resonance tubes (RT) is 1.5.

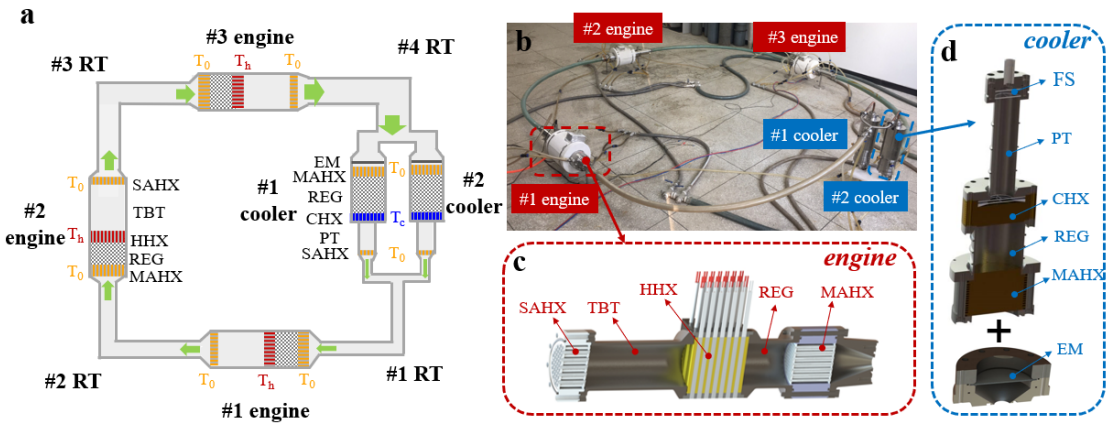

Figure 1. Experimental setup of the looped three-stage thermoacoustically-driven cooler: (a) schematic of the system (b) photo of the experimental setup (c) a thermoacoustic engine unit (d) a thermoacoustic cooler unit. The green arrows indicate acoustic power flow. The key components are: RT (resonance tube), SAHX (secondary ambient heat exchanger), TBT (thermal buffer tube), HHX (high-temperature heat exchanger), REG (regenerator), MAHX (main ambient heat exchanger), FS (flow straightener), PT (pulse tube), CHX (cold-temperature heat exchanger), EM (elastic membrane). The two paralleled thermoacoustic cooler units are connected by Y-type tubes.

Table 1. The dimensions of the main components of the system. All unitless dimensions are in millimeters (mm).

	Component	Diameter	Length	Other dimensions
Engine unit	MAHX	80	60	Shell-tube type, 20 % in porosity, 2 in hydraulic diameter
	REG		70	80% in porosity, 150-mesh, 52 μm in wire diameter
	HHX		80	Plated-fin type, 37 % in porosity, 1 in channel width
	TBT		150	5 in wall thickness

	SAHX		40	Shell-tube type, 43 % in porosity, 3 in hydraulic diameter
Cooler unit	MAHX	75	64	Plated-fin type, 26 % in porosity, 0.4 in channel width
	REG		70	70% in porosity, 300-mesh, 31 μm in wire diameter
	CHX		30	Plated-fin type,18 % in porosity, 0.25 in channel width
	PT	37	150	2.2 in wall thickness
	SAHX		9	40-mech cooper mesh
RT	1st	15	2400	1.5 in wall thickness
	2nd	18		
	3rd	22		
	4th	27		

Gedeon streaming [29] and jet-driven streaming [30] carry large time-averaged convective enthalpy fluxes from the hot end to the cold end that can degrade system performance. To reduce the jet-driven streaming, mesh flow straighteners were located at two ends of the pulse tube and thermal buffer tube, and a high-temperature heat exchanger with uniform flow was used (see Section 3.1). To suppress the Gedeon streaming, an elastic membrane was located at the inlet of each cooler unit. In addition to the above two streaming modes, the gravity-driven convective flow, influenced by the inclination angle of coolers and caused by buoyancy forces resulting from differences in gas density, also affects the cooler performance. By using a linear compressor to drive the thermoacoustic cooler unit, we compared cooling power at two typical inclination angles (Fig. 2a) to study the influence of the gravity-driven convective flow. When the cold end of the pulse tube was vertically below the ambient end (as θ=0° in Fig.2a), the gravity-driven convective flow can be entirely suppressed. In Figure. 2b, the experimental results showed that without the gravity-driven convective flow, cooling power was improved by more than 15%. Therefore, in the following experiments, both thermoacoustic cooler units were oriented vertically to avoid the gravity-driven convective flow.

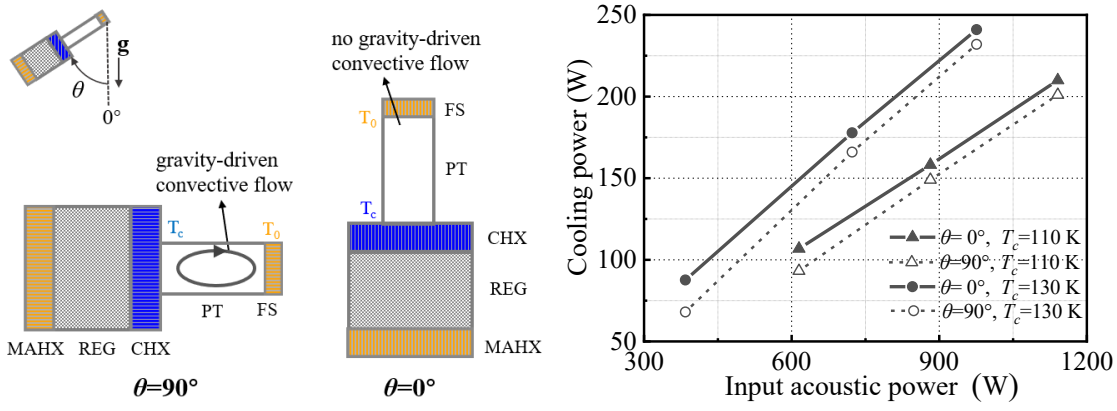

(a) (b)

Figure 2. Effect of the gravity-driven convective flow on the performance of the thermoacoustic cooler (a) two typical inclination angles (b) cooling performance. The experimental comparisons were conducted under the same operating conditions of a working frequency of 55 Hz and a mean pressure of 3 MPa.

2.2 Performance consistency of engine and cooler units

In the optimized design, the geometry of each energy-conversion unit (i.e. engine unit or cooler unit) is considered to be identical. However, in practice, it is difficult to achieve geometry uniformity due to the uncertainties in the machining and assembly accuracy. Such discrepancy will lead to deviation from the optimal design and therefore has a negative impact on the system performance. In this section, we tested each energy-conversion unit to see if their performance was consistent. The test platform of the engine unit consisted of a linear compressor, a linear alternator, and an engine unit. The property acoustic fields were obtained in each engine unit by adjusting the compressor and the alternator. Using the same input acoustic power from the compressor, the engine performance consistency was obtained by comparing output acoustic power. The experimental results showed that the performance consistency of the engine units exceeded 95%. The test platform of the cooler unit consisted of a linear compressor and a cooler (with an inertance tube and a gas reservoir). The performance consistency of the cooler was obtained by comparing cooling power under the same operating conditions. The experimental results demonstrated that the performance consistency of the cooler units was above 93%. The above results illustrate that both the engine and cooler unit performance have high consistency, which is essential for a high-performance overall system.

2.3 Measurements

Pressures, temperatures, and power were measured in the experiments. For pressure measurements, mean pressure was measured using a pressure transmitter (model JYB-KO-HVG), and dynamic pressures were measured by high-precision dynamic pressure sensors from PCB Piezotronics (model 113B26) which were installed at the inlets of each engine and cooler. All signals were collected and processed by dynamic signal acquisition cards (model NI PXI-4472) from National Instruments, and LabView was used to read the final data. For temperature measurements, the heating temperatures were measured by calibrated K-type sheathed thermocouples (model WRKK-103) which were located at the surfaces of each high-temperature heat exchanger. Cooling temperatures were measured by calibrated platinum-resistance thermometers with an accuracy of ±0.1 K (model PT100), which were inside each cold-temperature heat exchanger. All temperature signals were collected by a digital

multimeter (Keithley). For power measurements, the heating power of each high-temperature heat exchanger was measured by a three-phase power meter (Ainuo model AN7931X). Constantan wires heated by a direct-current power source were mounted on each cold-temperature heat exchanger to simulate the cooling power, which was measured by a direct-current wattmeter (Kikusui model PCR4000).

3 Experimental Results and Discussions

In the experiment, the system was charged with 7 MPa pressurized helium. The temperature of the circulating ambient water was 293 K. The cooling temperatures were within natural gas liquefaction temperature ranges. The regenerator, high-temperature heat exchanger, and thermal buffer tube of the engine units were enclosed in thermal insulation materials to reduce heat loss to the environment. Similarly, the regenerator, cold-temperature heat exchanger, and pulse tube of the cooler units were enclosed in a vacuum chamber to minimize heat loss to the environment. The onset temperatures of the system were around 500 K. The system exergy efficiency was defined as

$$\eta_{ex} = \frac{(Q_{c,1}+Q_{c,2})(\frac{T_0}{T_c}-1)}{(Q_{h,1}+Q_{h,2}+Q_{h,3})(1-\frac{T_0}{T_h})} \tag{1}$$

where Q_c and Q_h are the cooling power and input heating power in an engine and cooler unit, respectively. T_c, T_h, and T_0 are the cooling temperature, heating temperature, and ambient temperature, respectively. The numbers 1, 2, and 3 represent the corresponding stage number of the unit.

3.1 Comparison of two high-temperature heat exchangers with different flow uniformity

The HHX is one of the core components of the thermoacoustic system. The function of the HHX is to transfer time-averaged heat from an external heat source to the working gas via thermal fluids. The HHX should be designed to provide good thermal contact between two flow streams, as heat exchange effectiveness directly influences the system cooling performance. However, effective heat exchange is not always enough for the high performance of the system, because the nonuniform oscillating flow at the outlet of HHX can lead to a significant exergy loss resulting from mixing hot and cold gases in an adjacent thermal buffer tube. In this section, we compared two plated-fin HHXs which have similar heat transfer effectiveness but different flow uniformities.

One of the heat exchangers (Type-A) is shown in Figure 3a. In this HHX type, holes were drilled in a copper block to allow tubes to pass through as thermal fluid

channels. The fins were machined by wire electrical discharge machining with desired spacings for gas flow. The thermal fluids transferred heat to the fins via the tube walls and further transferred it to the oscillating gas flow in the thermoacoustic engine. However, for this configuration, the gas flow cannot be distributed evenly when leaving the HHX due to blockage of the thermal fluid channels (see the rightmost figure in Fig.3a). This non-uniform gas flow can easily induce significant jet-driven streaming in the thermal buffer tube, which will cause the mixing of hot gas and ambient gases, resulting in huge exergy loss. Unfortunately, since the block channels occupy large areas, it is difficult to make the gas flow uniform even if flow straighteners are used. In contrast, another type of heat exchanger (Type-B) is shown in Figure 3b. The fins, made from thin copper sheets, were cut to different lengths and arranged at regular intervals to form gas flow channels. The desired spacings between fins were maintained by small copper spacers between each pair of fins, and good thermal contacts between the spacers, fins, and tubes were ensured by welding. Each of the fins had holes drilled to accept the tubes containing thermal fluids. Compared to Type-A HHX, Type-B HHX can easily achieve much uniform flow at its outlet simply as long as a layer of flow straightener is installed (see the rightmost figure in Fig.3b). The uniform flow to the thermal buffer tube can reduce the mixing of hot and ambient gases and significantly improve the system performance.

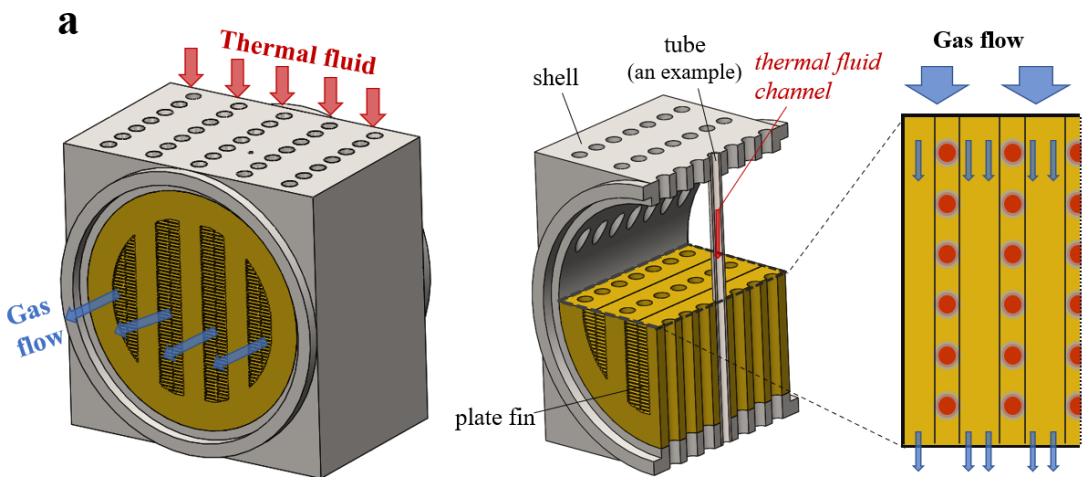

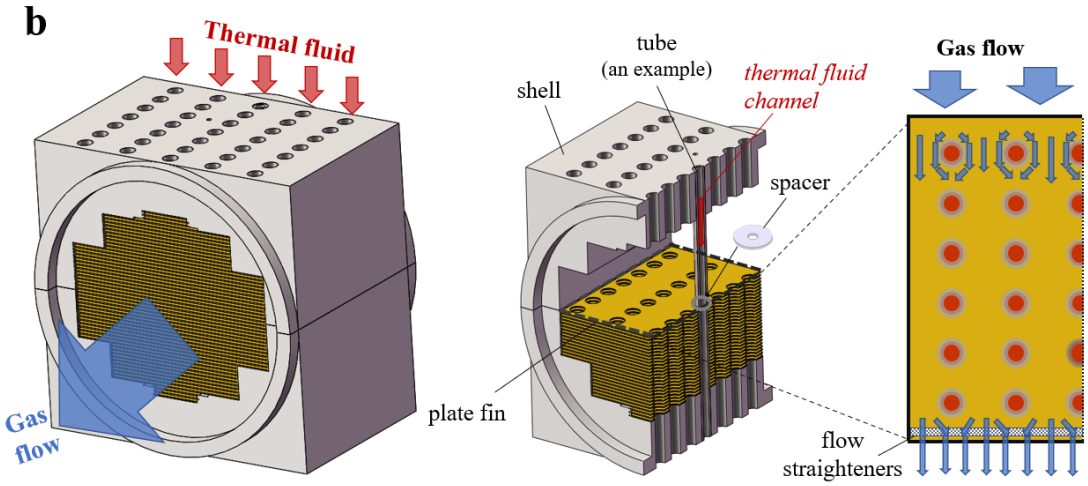

Figure 3. Two types of plated-fin high-temperature heat exchangers with different flow uniformities at its outlet: (a) Type-A with non-uniform flow; (b) Type-B with uniform flow. The figure only shows an example of a tube rather than all tubes. In the experiments, electric heating rods were inserted in the thermal fluid channels acting as heat sources.

Experiments were performed to compare the overall system performance by using the two HHXs. The working conditions, as well as the dimensions of other components, remained the same. To remove the influence of heat exchange effectiveness, two determining parameters of the two HHXs—porosities (area of the gas channel to cross-sectional area) and hydraulic diameters (spacing between two fins)—were both maintained at about 37 % and 1 mm, respectively. Meanwhile, the two HHXs were both 80 mm in diameter and 80 mm in length. These same parameters enable the two HHXs to have similar heat transfer capabilities, so that flow uniformity becomes the main determinant of the performance. Figure 4 shows the comparison results of the overall system performance using the two HHXs. The experimental results represent significant increases by 28% in cooling power and 33 % in overall system exergy efficiency when using the HHX with uniform flow (Type-B HHX). Therefore, in the following sections, the overall system performance using the Type-B HHX will be presented.

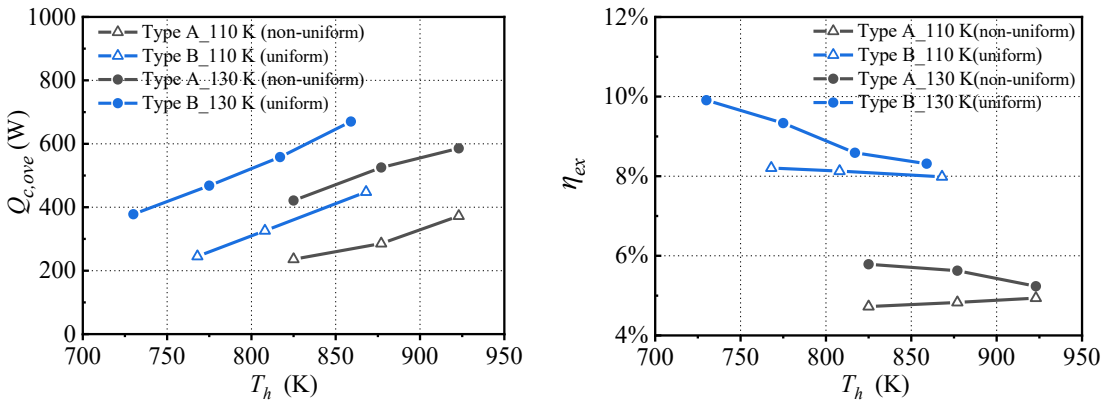

(a) (b)

Figure 4. Experimental results of the overall system performance of (a) overall cooling power (b) system exergy efficiency, when using the two HHXs with different flow uniformity. The experiments were conducted under different heating temperatures (T_h) and cooling temperatures of 110 K and 130 K.

3.2 Effect of operating temperatures

The heating temperature is crucial to determining the power amplification ratio of an energy-conversion unit. Figure 5 presents the effects of heating temperatures on system performance at a cooling temperature of 130 K. According to Figure 5a, the heating temperature has almost no effect on working frequency, because the working frequency is mainly determined by the component dimensions, especially by the length of the resonance tubes. Figure 5b shows that the input heating power increases with the heating temperature and with the engine stage number, due to the cascade-amplified acoustic power in the increased engine stages. At the maximum heating temperature, the input heating power for the 1st, 2nd and 3rd engine units are 2659 W, 4044 W and 8672 W, respectively. Figure 5c shows that the difference between the cooling power of the 1st and the 2nd cooler is within 7%, as expected with good performance consistency. Figure 5d shows that the overall system achieved the highest system exergy efficiency of 10% at a heating temperature of 730 K; when the heating temperature increased to 859 K, the system exergy efficiency decreased to 8.4 %. The calculated results obtained by the SAGE program [31] were compared with the experimental results. The difference between the calculated and experimental results for frequency were within 5%. The calculated input heating power was higher than experimental results, and their discrepancy increased with the increasing heating temperature. The experimental results of cooling power and efficiency were both lower than the calculated results by up to 50%. The possible reasons for the discrepancies are discussed in detail in Section 4.

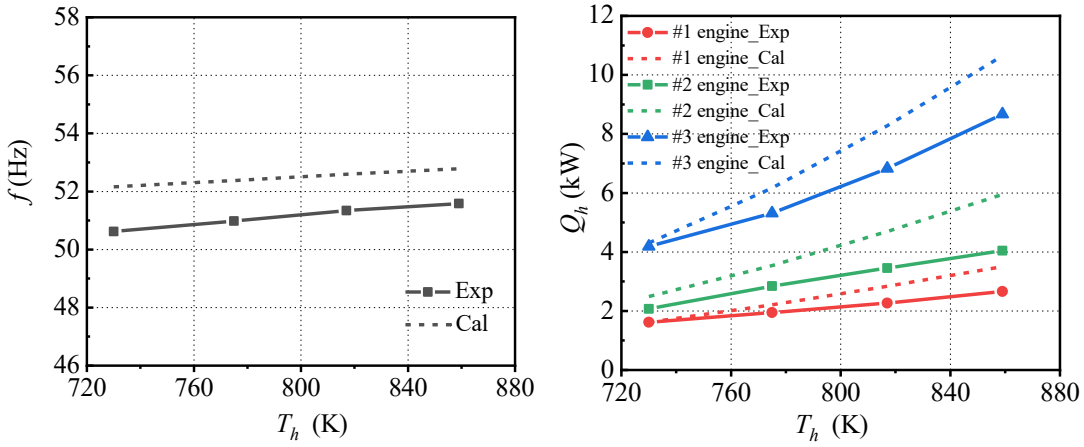

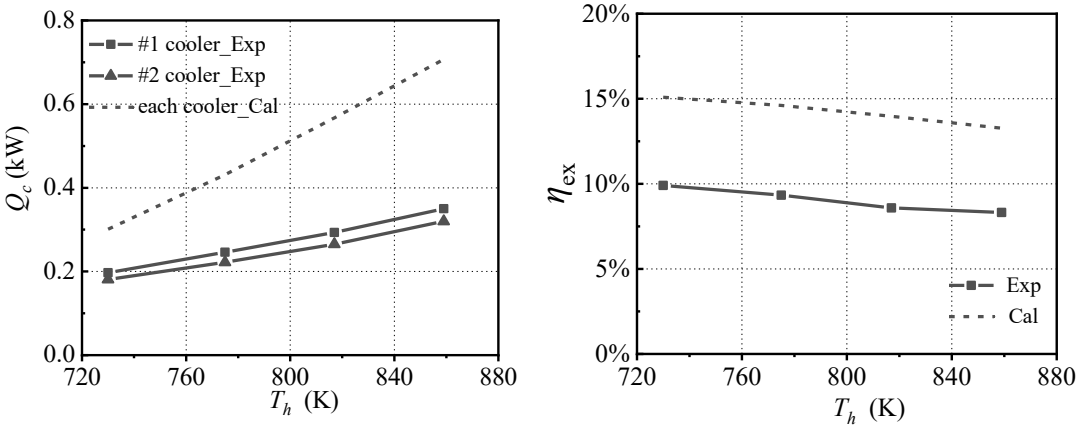

(c) (d)

Figure 5. Experimental and calculation results of the system performance of: (a) working frequency (b) input heating power in each engine unit (c) cooling power in each cooler unit (d) system exergy efficiency, under different heating temperatures. The cooling temperature is fixed at 130 K.

The natural gas liquefaction temperature varies according to changes in pressure on a gas. Therefore, the system performance at two typical cooling temperatures of 110 K and 130 K were studied, as presented in Figure 6. The increased cooling temperature contributes to the larger overall input heating power. The maximum overall heating power is 15.3 kW when the cooling temperature is 130 K. The system has high efficiency within the range of 8% to 10 % at natural gas liquefaction temperature ranges: in the most efficient condition, the overall system can achieve an exergy efficiency of 10% and a cooling power of 378 W; in the largest capacity condition, the overall system can achieve a cooling power of 670 W and exergy efficiency of 8.3%.

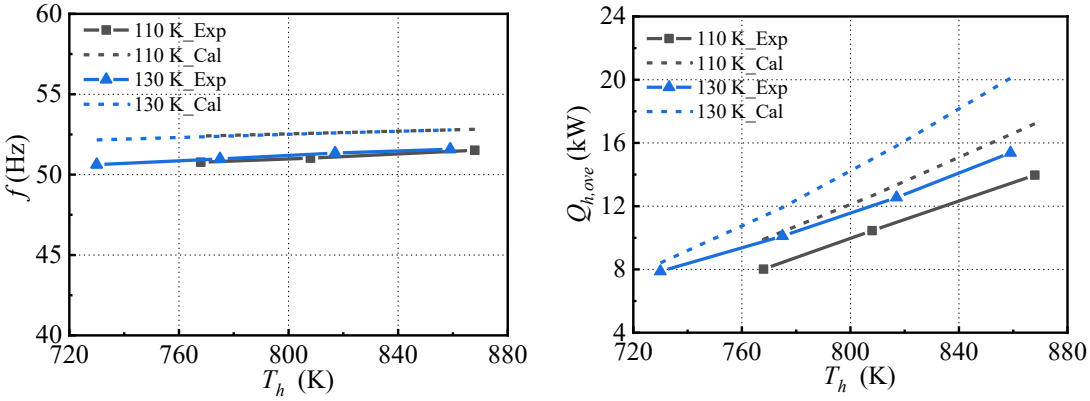

(a) (b)

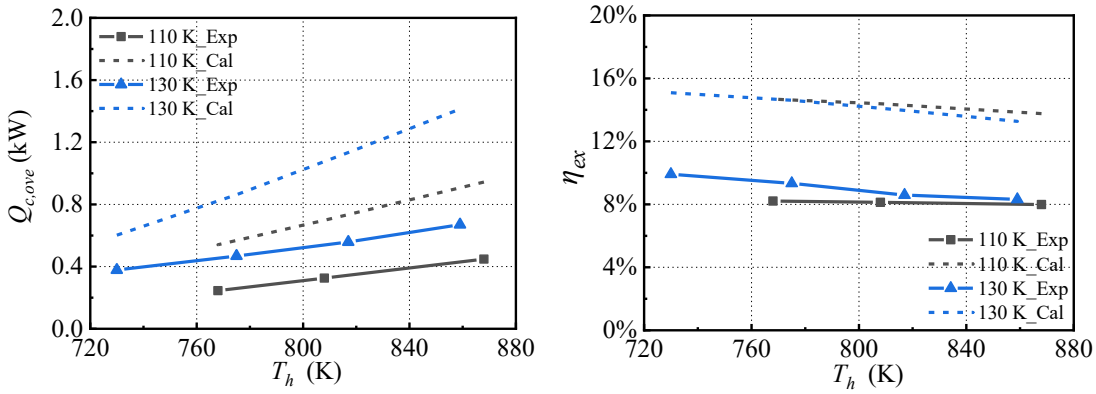

(c) (d)

Figure 6. Experimental and calculation results of the system performance of (a) working frequency (b) overall input heating power (c) overall cooling power (d) system exergy efficiency, under different heating temperatures and cooling temperatures of 110 K and 130 K.

3.3 Utilization of variable-temperature heat sources

Heat utilization is always accompanied by a drop in temperature of the heat transfer thermal fluid. The experiments described above were performed on the system with identical heating temperature in each engine unit, without considering external exergy loss between the thermal fluid and heat exchanger. Given an initial hot thermal fluid, the smallest external exergy loss between the thermal fluid and heat exchanger can be realized by organizing heat flows across heat exchangers with the minimum temperature drop compatible with the technically feasible heat exchange areas. Cascade systems with variable heating temperatures offer just such an opportunity, where the decreasing temperatures of the thermal fluid can be used in increasingly lower temperature heat exchangers. Figure 7 shows the thermoacoustic engine for such purpose, where the thermal fluid can be cascade utilized in multiple engine units by gradually decreasing the heating temperatures, i.e., $T_{h1}<T_{h2}<T_{h3}$. The system exergy efficiency at variable heating temperatures was defined as

$$\eta_{ex}=\frac{(Q_{c,1}+Q_{c,2})(\frac{T_0}{T_c}-1)}{Q_{h,1}(1-\frac{T_0}{T_{h,1}})+Q_{h,2}(1-\frac{T_0}{T_{h,2}})+Q_{h,3}(1-\frac{T_0}{T_{h,3}})} \quad (2)$$

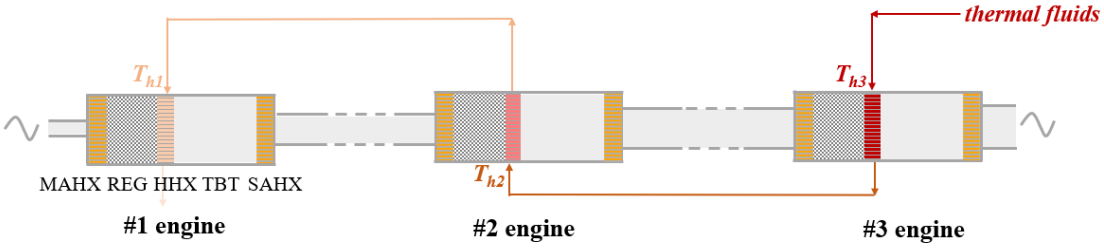

Figure 7. A thermoacoustic engine for cascade utilization of a variable-temperature heat source. The thermal fluid first passes through the 3rd engine unit. The heating temperatures of the engine units decrease with the decreased stage number (i.e. $T_{h1}<T_{h2}<T_{h3}$).

Experiments were conducted to explore the system performance at variable heating temperatures. Figure 8 shows the system performance when $T_{h,1}$, $T_{h,2}$, and $T_{h,3}$ are 673 K, 773 K, and 873 K, respectively. When operating at variable heating temperatures, the system can still display comparable system exergy efficiency to the identical-temperature system. In addition to its competitive energy conversion efficiency, the system is also favorable for reducing the external exergy loss between the heat source and the heat exchanger. In the future, it is expected that this system exergy efficiency can be further improved by optimizing the component dimensions for different heating temperatures.

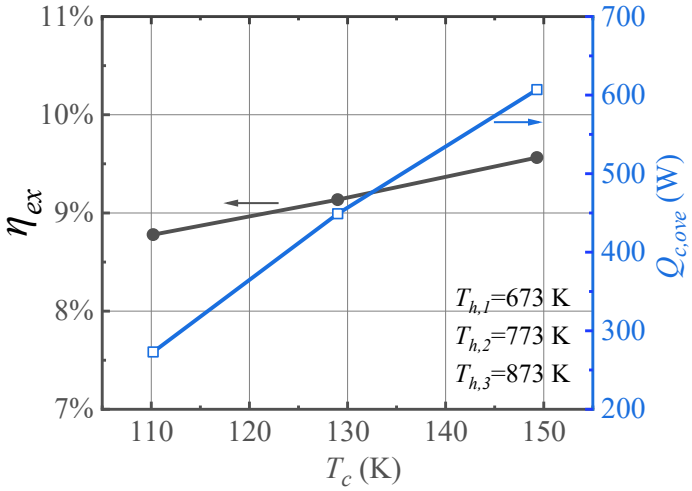

Figure 8. Experimental results of system exergy efficiency and overall cooling power at the variable heating temperatures of 873 K, 773 K, 673 K for the 3rd, 2nd, 1st engine unit, respectively. The cooling temperature is 150 K.

3.4 Comparisons with existing thermoacoustically-driven cryocoolers

Table 2 compares the performance of the proposed system with existing thermoacoustically-driven cryocoolers. Ref. 24 represents a double standing-wave thermoacoustic engine coupled to an orifice-type thermoacoustic cooler. Ref. 32 reports a looped traveling-wave engine incorporating a cooler in a loop, which is similar to the proposed system, but with identical-diameter resonance tubes. Ref. 27 reports a looped traveling-wave engine with a cooler connected at the branch of each engine unit. According to the comparison results, the proposed system achieves a record of the highest exergy efficiency compared to the previous thermoacoustically-driven cryocoolers. When compared to the system in Ref. 32, the proposed system improves efficiency by 50 % thanks to the different-diameter resonance tubes. When compared

to the previous record-holder system in Ref. 27, the proposed system represents a 25 % improvement in efficiency.

For future work, the proposed system is expected to achieve higher efficiency by using an integrated cooler instead of two parallel coolers, which is favorable for reducing the power loss of the Y-type connect tubes. At the same time, by changing the size of the system, the cooling power is expected to scale up to the order of kilowatts.

Table 2. Experimental comparisons of the performance between the proposed system with the existing thermoacoustically-driven cryocoolers.

Years	Organization	engine stage	P_m (MPa)	f(Hz)	T_h (K)	T_c (K)	$Q_{c,\,all}$ (W)	η_{ex}	Ref.
1998	Los Alamos National Laboratory	1-stage	3.0	40	-	125	2100	5.8 %	24
2010	Aster Thermoacoustic	3-stage	2.7	95	512	227	95	6.6 %	32
2015	Chinese Academy of Sciences	3-stage	7.0	55	903	130	1200	8.0 %	27
2020	Chinese Academy of Sciences	3-stage	7.0	51	730	130	378	10.0 %	This work

4 Discussion on the experiment and calculation results

In this section, the discrepancy between the experimental and calculation results is discussed. The two sets of results are quantitatively different although they are qualitatively in agreement. The possible reasons for the differences include but are not limited to the following aspects:

(1) Limited heat transfer model

Two limitations in the heat transfer model of the Sage program contribute to the discrepancy. Firstly, Sage is a one-dimensional model that averages radial variations. This means that the program cannot capture the details of temperature changes across the heat exchanger and instead must rely on previously obtained corrections for heat transfer under given mean conditions. Yet for a transferred heat of 2 kW in a typical plate-finned heat exchanger, the radial temperature difference has been reached as over 20 K [33]. Secondly, the Sage program uses semi-empirical terms for the friction factor, Nusselt number, and axial conductivity ratio, which may deviate from actual practical conditions. Figure 9 shows the experimental and calculated results of gas temperatures in the MAHX of the thermoacoustic cooler. The gas temperature at the inlet of the MAHX was measured by thermocouples, and the gas temperature at the outlet of the MAHX (see the inserted star) was inferred from the measured axial temperature

distribution in the REG. The results show that the calculated temperatures are about 10 K lower than the experimental values due to the limited heat transfer model.

Developing improved two-dimensional models and correcting empirical terms for different cases are further steps that could improve the current calculation model.

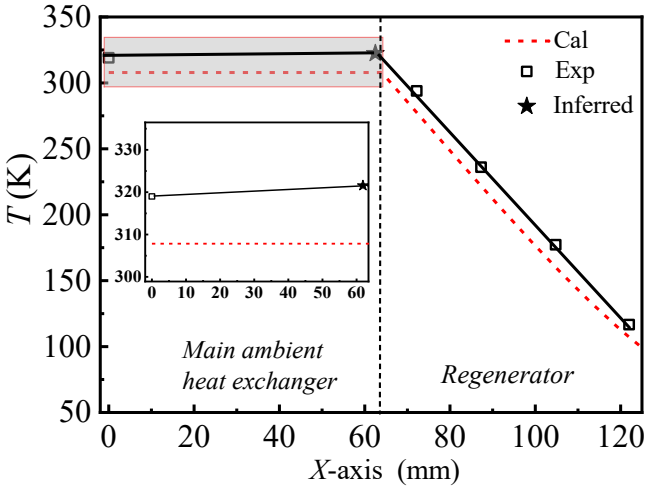

Figure 9. Experiment (Exp) and calculation (Cal) of gas temperatures at the inlet and outlet of the thermoacoustic cooler unit. Inset shows zoomed in grayed region. The inserted star point is inferred from the experimental axial temperature distribution in the regenerator.

(2) Static heat losses

Static heat losses refer to the heat loads required to maintain the heating temperature when the thermoacoustic system is not working. A thermoacoustic system can be affected by three kinds of static heat losses: solid conductive heat loss (in axial and radial directions), $\Delta Q_{sol,cnd}$, gas conductive heat loss, $\Delta Q_{gas,cnd}$, and gravity-driven convective heat loss, $\Delta Q_{gra,cnv}$. Compared with solid conductive heat loss $\Delta Q_{sol,cnd}$, gas conductive heat loss $\Delta Q_{gas,cnd}$ can be neglected because of the much smaller thermal conductivity of gas (thermal conductivities for helium and stainless steel are 0.152 W/m·K and 14.4 W/m·K at 300 K, respectively). In this section, experiments were conducted on the thermoacoustic engine unit to measure the $\Delta Q_{sol,cnd}$ and $\Delta Q_{gra,cnv}$ under different heating temperatures. The engine unit was oriented horizontally as previously, and its inlet and outlet were blocked to form a high-pressure environment. $\Delta Q_{sol,cnd}$ and $\Delta Q_{gra,cnv}$ were respectively obtained by the following steps for one heating temperature: (1) Measure input heating power to the engine unit when it was filled with 7 MPa helium. The value of the input heating power equals total static heat losses, i.e. $\Delta Q_{sol,cnd}+\Delta Q_{gra,cnv}$; (2) Measure input heat power when the engine was under complete vacuum to remove the influence of gas gravity-driven convection. The value of the input heating power equals $\Delta Q_{sol,cnd}$; (3) The difference between the above two values of the input heating power corresponds to $\Delta Q_{gra,cnv}$.

Figure 10 compares the experimental and calculated results of the static heat losses at different heating temperatures. The results show that there are significant differences between the Sage model and the experimental values for the static heat losses. The discrepancy in the solid conductive heat loss occurs because the radial solid conductive heat loss is ignored in the Sage program, although the axial solid conductive heat loss has been well considered. The reason for the discrepancy in the gravity-driven convective heat loss is that, the Sage program uses a semi-empirical correlating expression of the gravity-driven convection enhancement according to experimental data of a cylinder with adiabatic walls [34], which may deviate from the current practical conditions.

Two methods can be suggested to reduce the static heat losses in the experiments. Firstly, the high-temperature components in the engine should be enclosed in low-thermal-conductivity materials (e.g. alumina fiber blanket), to reduce the radial conductive heat loss to the environment. Secondly, it is better to place the ambient end of the thermal buffer tube vertically below the hot end to avoid gravity-driven convection loss.

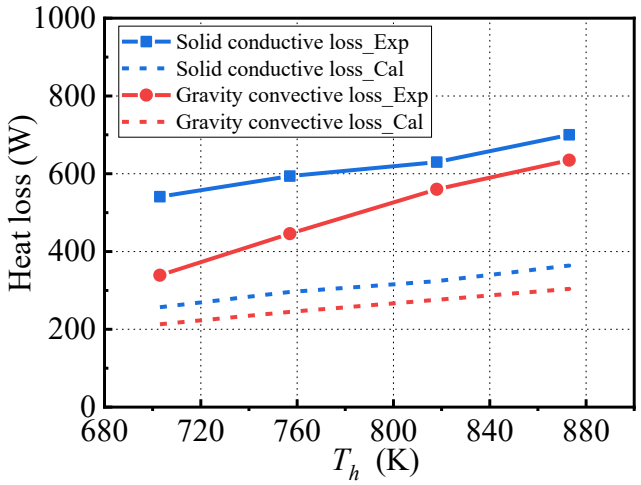

Figure 10. Comparison of experimental and calculation results for the solid conductive heat loss and gravity-driven convective heat loss in the thermoacoustic engine unit. The calculation results are obtained from the Sage program.

(3) Acoustic streaming

Acoustic streaming usually refers to a steady mass-flux of density or velocity, usually of second order, that is superimposed on the larger first-order oscillating acoustic mass-flux density or velocity and that is driven by the first-order oscillations [30]. Based on the mechanism by which streaming is generated, there are three types of acoustic streaming in a thermoacoustic system: Rayleigh streaming, jet-driven streaming, and Gedeon streaming. Rayleigh streaming is driven by viscous and thermal boundary layer effects and is generated within the thermal and viscous penetration

depths. Jet-driven streaming occurs when there are periodic suction and ejection of a viscous fluid through a sudden change in cross section. Gedeon streaming refers to a non-zero net mass transport involving a phase difference between the acoustic velocity and density wave in a loop. The acoustic streaming carries a large heat flux from the hot to the cold end and produces issues: in the thermoacoustic engine, the carried heat is considered as a loss of the heat from the heat source without participating in the thermoacoustic process; in the thermoacoustic cooler, the delivered heat to the cold end becomes a loss of cooling power. While Gedeon streaming is considered in the Sage program, neither Rayleigh nor Jet streaming is not well accounted for in the Sage model, which is another reason for discrepancies between experiments and calculations.

5 Conclusions

In this paper, we report an experimental investigation of a highly efficient looped traveling-wave thermacoustically-driven cryocooler at natural gas liquefaction temperature ranges. The paper presents detailed experimental performance as well as comparisons between the experiments and calculations. The following conclusions can be drawn from the results:

(1) The proposed thermoacoustically-driven cryocooler outperforms the existing similar thermoacoustic systems in terms of efficiency. The experiments illustrated that for a heating temperature of 730 K, the proposed system can achieve an overall exergy efficiency of 10 % and a cooling power of 378 W. This represents a 25% improvement in efficiency with respect to the previous best system.

(2) The flow uniformity of the heat exchanger is found to be a crucial factor in determining system performance. The experimental results represent an improvement of 33% in system exergy efficiency and 28% in cooling power when using the heat exchanger with uniform flow.

(3) The proposed system displays a high exergy efficiency of over 9 % when operating at variable heating temperatures, which shows great potential in cascade utilization of heat.

(4) The reasons for the difference between experiments and calculations include, but are not limited to, limited heat transfer model, inaccurate static heat losses, and some neglected acoustic streaming losses.

This paper combined with Ref. 28 forms a complete study of a highly efficient thermoacoustically-driven cryocooler. The developed prototype achieved a record efficiency with respect to existing similar thermoacoustic systems, and therefore shows promising prospects in the application of natural gas liquefaction.

Acknowledgments

This work was supported by National Key Research and Development Program of China (Grant No. 2016YFB0901403), National Natural Science Foundation of China (Grant No. 51906250, No. 51876213), Beijing Natural Science Foundation (Grant No. 3194061), Strategic Priority Research Program of the Chinese Academy of Sciences (Grant No. XDA 21080300, No. XDC 03050101).

References

[1] S. Mokhatab, J.Y. Mak, J.V. Valappil, D.A. Wood. Handbook of liquefied natural gas. Gulf Professional Publishing, 2013, Oxford.

[2] P. Stevens. The 'Shale Gas Revolution': Hype and Reality. A Chatham House Report, 2010. Available at: https://pdfs.semanticscholar.org/586e/821194e40d2aca40dd13de56849cad6a844a.pdf. (accessed: 15th June 2020).

[3] C. Song, S. Tan, F.C. Qu, W.D. Liu, Y. Wu. Optimization of mixed refrigerant system for LNG processes through graphically reducing exergy destruction of cryogenic heat exchangers. Energy 2019; 168:200–206.

[4] M.A. Qyyum, F. W, A. Hussain, A.A. Noon, M. Lee. An innovative vortex-tube turbo-expander refrigeration cycle for performance enhancement of nitrogen-based natural-gas liquefaction process. Applied Thermal Engineering 2018; 144: 117–125.

[5] B. Ghorbani, M.H. Hamedi, M. Amidpour, M. Mehrpooya. Cascade refrigeration systems in integrated cryogenic natural gas process (natural gas liquids (NGL), liquefied natural gas (LNG) and nitrogen rejection unit (NRU)). Energy 2016; 115: 88–106.

[6] H. Sanavandi, M. Mafi, M. Ziabasharhagh. Normalized sensitivity analysis of LNG processes-Case studies: Cascade and single mixed refrigerant systems. Energy 2019; 188: 116068.

[7] Y. Zhao, Z. Yang, E. Luo, Y. Zhou. Travelling-wave thermoacoustic high-temperature heat pump for industrial waste heat recovery. Energy 2014; 77: 397–402.

[8] J. Xu, E. Luo, S. Hochgreb. Study on a heat-driven thermoacoustic refrigerator for low-grade heat recovery. Applied Energy 2020; 271: 115167. https://doi.org/10.1016/j.apenergy.2020.115167.

[9] P. Saechan, A.J. Jaworski. Thermoacoustic cooler to meet medical storage needs of rural communities in developing countries. Thermal Science and Engineering Progress 2018; 7: 164–175.

[10] J. Xu, J. Hu, L. Zhang, E. Luo. A looped three-stage cascade traveling-wave thermoacoustically-driven cryocooler. Energy 2016; 112: 804–809.

[11] T. Bi, Z. Wu, L. Zhang, G. Yu, E. Luo, W. Dai. Development of a 5 kW traveling-wave thermoacoustic electric generator. Applied Energy 2017; 185: 1355–1361.

[12] K. Wang, D. Sun, J. Zhang, Y. Xu, K. Luo, N. Zhang, J. Zou, L. Qiu. An acoustically matched traveling-wave thermoacoustic generator achieving 750 W electric power. Energy 2016; 103: 313–321.

[13] Z. Wu, G. Yu, L. Zhang, W. Dai, E. Luo. Development of a 3 kW double-acting thermoacoustic Stirling electric generator. Applied Energy 2014; 136: 866–872.

[14] J. Wheatley, A. Cox. Natural engines. Physics Today 1985; 38(8): 50–58.

[15] G.W. Swift. Analysis and performance of a large thermoacoustic engine. The Journal of the Acoustical Society of America1992; 92(3): 1551–1563.

[16] J. Olson, G.W. Swift. A loaded thermoacoustic engine. The Journal of the Acoustical Society of America 1995; 98(5): 2690–2693.

[17] R.L. Chen, S.L. Garrett. Solar/heat driven thermoacoustic engine. The Journal of the Acoustical Society of America 1998; 103(5): 2841.

[18] S. Backhaus, G.W. Swift. A thermoacoustic-Stirling heat engine: Detailed study. The Journal of the Acoustical Society of America 2000; 3148–3166.

[19] S. Backhaus, G.W. Swift. A thermoacoustic-Stirling heat engine. Nature 1999; 399: 335–338.

[20] M.E.H. Tijani, S. Spoelstra. A high performance thermoacoustic engine. Journal of Applied Physics 2011; 110:093519.

[21] de Blok K. Novel 4-stage traveling wave thermoacoustic power generator. In: ASME 2010 3rd Joint US-European fluid engineering summer meeting collocated with 8th international conference on nanochannels, microchannels, and minichannels. American Society of Mechanical Engineers, vol. 7; 2010. p. 73–9.

[22] T. Jin, R. Yang, Y. Wang, Y. Feng, K. Tang. Low temperature difference thermoacoustic prime mover with asymmetric multi-stage loop configuration. Scientific Reports 2017; 7: 7665.

[23] M. Senga, S. Hasegawa. Four-stage loop-type cascade traveling-wave thermoacoustic engine. Applied Thermal Engineering 2016; 104: 258–262.

[24] B. Arman, J.J. Wollan, G.W. Swift, S. Backhaus. Thermoacoustic natural gas liquefiers and recent developments. Cryogenic and refrigeration proceedings of ICCR. Hang Zhou, International Academic Publisher and World Publishing Corporation (2003), 123–127.

[25] B. Arman, J.J. Wollan, V. Kotsubo, S. Backhaus, G. Swift. Operation of thermoacoustic Stirling heat engine driven large multiple pulse tube refrigerator. R.G. Ross Jr. (Ed.), Cryocooler 13, Springer Science and Business Media Inc., New York (2004), 181–187.

[26] J. Xu, L. Zhang, J. Hu, Z. Wu, T. Bi, W. Dai, E. Luo. An efficient looped multiple-stage thermoacoustically-driven cryocooler for liquefaction and recondensation of natural gas. Energy 2016; 101: 427–433.

[27] L. Zhang, J. Hu, Z. Wu, E. Luo, J. Xu, T. Bi. A 1 kW-class multi-stage heat-driven thermoacoustic cryocooler system operating at liquefied natural gas temperature range. Applied Physics Letters 2015; 107: 033905.

[28] J. Xu, J. Hu, E. Luo, L. Zhang, W. Dai. A cascade-looped thermoacoustic driven cryocooler with different-diameter resonance tubes. Part I: Theoretical analysis of thermodynamic performance and characteristics. Energy 2019; 181: 943–953.

[29] D. Gedeon. DC gas flow in Stirling and pulse-tube cryocoolers. Cryocooler 1997; 9: 385–392.

[30] G.W. Swift. Thermoacoustics: a unifying perspective for some engines and refrigerators. Acoustical Society of America 2002.

[31] D. Gedeon. SAGE: object-oriented software for cryocooler design. Cryocoolers 8 1995; 281–292.

[32] de Blok K. Multi-stage travelling wave thermoacoustic in practice. In 19th International Congress on Sound and Vibration Vilnius, Lithuania: International Institute of Acoustics and Vibration (IIAV) and Vilnius University; 2012. p. 1–8.

[33] J. Xu, J. Hu, L. Zhang and E. Luo. A novel shell-tube water-cooled heat exchanger for high-capacity pulse-tube coolers. Applied Thermal Engineering 2016; 106: 399–404.

[34] D.K. Edwards, I. Catton. Prediction of heat transfer by natural convection in closed cylinders heated from below. International Journal of Heat and Mass Transfer 1969; 12 (1): 23–30.